Journal of Molecular Liquids, Volume 367, Part B, December 2022, Article number 120486
DOI:10.1016/j.molliq.2022.120486

Influence of pipeline steel surface on the thermal stability of methane hydrate

Guozhong Wu [a, b, 1, *], Linqing Tian [b, 1], Li Ha [b], Feng Feng [b], Zhifeng Yang [a], Jing-Chun Feng [a, c], Frederic Coulon [d], Yuelu Jiang [b], Ruifeng Zhang [e]

[a] School of Environment, Ecology and Resources, Guangdong University of Technology, Guangzhou 510006, China

[b] Institute for Ocean Engineering, Shenzhen International Graduate School, Tsinghua University, Shenzhen 518055, China

[c] Research Centre of Ecology & Environment for Coastal Area and Deep Sea, Guangdong University of Technology & Southern Marine Science and Engineering Guangdong Laboratory (Guangzhou), Guangzhou 510006, China

[d] School of Water, Energy and Environment, Cranfield University, MK43 0AL, UK

[e] Shenzhen Qihay Academy Science and Technology Co., Ltd., Shenzhen 518055, China

* Corresponding Author

Email: wgz@gdut.edu.cn

[1] These authors contributed equally to this work

Graphical abstract

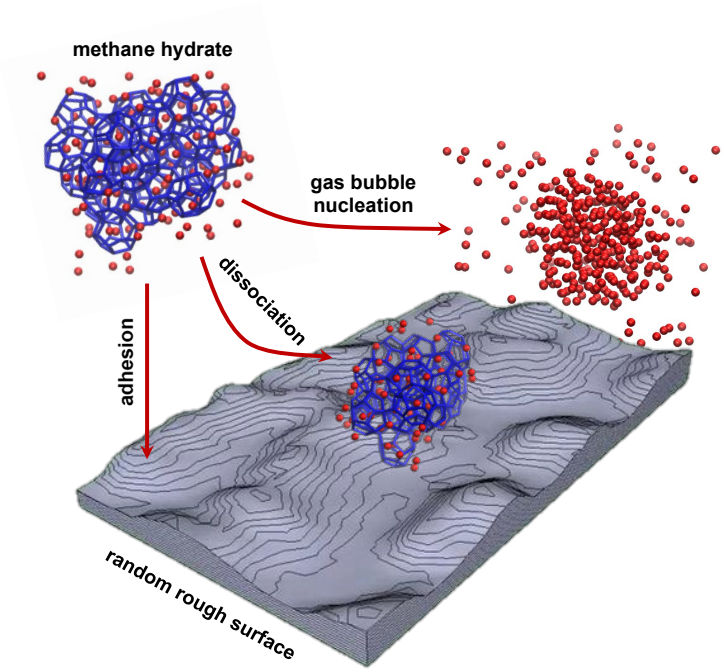

Abstract

The thermal stability and surface adhesion of natural gas hydrate are critical for the safety of oil and gas pipelines. The roughness and hydrophobicity of the pipe surface often vary during long-distance transportation, but it remains unclear about how these variances influence the hydrate stability. In this study, twelve molecular models of solid steel pipeline surfaces with random morphology were evaluated and molecular dynamics simulations were performed to gain insights into the kinetics of methane hydrate dissociation, the nucleation and growth of gas bubbles during hydrate decomposition, and the free energy of hydrate adhesion to the solid steel surface. Results demonstrated that the stability of methane hydrate could be decreased by up to 85% by increasing the hydrophobicity of the pipe surface by 52%. The bubble nucleation site of the gas released from hydrate decomposition shifted from bulk water to the solid surface by increasing the surface hydrophobicity (ε_{sw}: 3.73 ~ 5.74 kJ mol^{-1}), but a highly hydrophobic surface (ε_{sw}: 2.73 kJ mol^{-1}) made it hard to form gas bubble on either smooth or rough surface. Moreover, the free energy of hydrate adhesion also depended on the roughness and hydrophobicity of the solid surface, while the largest energy barrier for the adhesion of methane hydrate was found on the hydrophobic surface with high roughness. The findings from this study provided theoretical support for better understanding the methane hydrate evolution principles when the surface properties of the pipe wall changed from naturally occurred events (e.g., metal corrosion) or artificial treatment (e.g. chemical coating).

Keywords: methane hydrate; roughness; hydrophobicity; thermal stability; adhesion

1. Introduction

Natural gas hydrate formation during oil-gas transportation have plagued the petroleum industry for several decades, because it can decrease the circulation area and increase the flow resistance or even lead to the blockage and destruction of the well bore, pipeline and equipment (Shi et al., 2021). The hydrate plugging in the pipeline is a complex dynamic process including the nucleation and growth of hydrate crystals to particles, the continuous aggregation of hydrate particles, and the adhesion and gravity settlement of hydrate particles to the pipe wall (Zhang et al., 2021). Hydrate blockage must be removed in time to ensure flow security during oil-gas production and transportation. The heating and in-situ heat generation techniques with the advantages of low cost and high flexibility of practice have been widely applied in the petroleum industry to reduce the viscosity of heavy oil, which have also been introduced to remove gas hydrate (Wei et al., 2022). Natural gas hydrate are non-stoichiometric crystalline compounds in which methane molecules are trapped in the water cages formed by hydrogen bonds (Sloan and Koh, 2007). The hydrate will lose stability and the cages decompose into water and gas upon temperature rising. It is possible for the released gas to reform hydrate as the reformation of hydrate cages frequently occurs during hydrate dissociation (Yagasaki et al., 2014). If the gas concentration approaches the limit of super-saturation during hydrate decomposition, gas bubbles will form which play critical role on the dissociation or the secondary nucleation of hydrate. For example, Kuang et al. (2019) demonstrated that the hydrate tended to nucleate firstly at the bubble surface. Uddin and Coombe (2014) demonstrated that gas bubbles decreased

the hydrate decomposition rate by influencing the heat transfer, but other studies indicated that gas bubbles accelerated hydrate decomposition by absorbing the surrounding methane molecules and reducing the resistance for methane release or destabilizing the hydrate nuclei by disordering water structure (Yagasaki et al., 2014; Ji et al., 2018; Chen et al., 2021). There is no consistent conclusion on this issue which required more efforts to gain insights into the evolution of gas bubbles during hydrate dissociation.

One of the key factors influencing the gas hydrate stability and the gas bubble evolution is the physical and chemical characteristics of the pipeline surface, which do not keep constant but vary with time in the complex fluid flow environment during oil-gas pipeline transportation. For example, the chemical and microbiological corrosion will change the physical morphology of the pipeline surface. We found that the methane hydrate nucleation was strongly facilitated when the carbon steel surface was corroded, which was mainly resulted from the formation of convex and concave structure on the metal surface (Hu et al., 2018). Other recent studies also demonstrated that the changes in the roughness of the pipeline steels surface and the composite structured surface significantly altered the hydrate adhesion and decomposition properties (Zhang et al., 2021, 2022). However, to date there is limited information available on how the surface roughness of steel pipes would influence the thermal stability of gas hydrate. Molecular dynamics (MD) simulation is a versatile tool to gain insights into such microscopic mechanisms. A number of studies have been carried out to investigate hydrate formation and dissociation process using MD simulation, but the solid surface was

often modelled using a smooth surface or a rough surface with very regular groove structure (Ji et al., 2016; Hu et al., 2018; Ji et al., 2018; Zi et al., 2018; Das et al., 2022). These models were oversimplified as the morphology of the solid surface in the reality are often irregular. It requires future works to shed light on the molecular mechanisms for hydrate stability changes against temperature on the rough solid steel surface with random morphology. Furthermore, to the best of the authors' knowledge, there are no studies that have investigated how steel surface roughness of pipes influences gas bubble formation during hydrate decomposition and how it affects the energy barrier for the adhesion of hydrate particles onto the pipe surface.

Another critical property governing the gas hydrate evolution during the oil-gas transportation is the hydrophobicity of the solid surface (Nguyen et al., 2020). In the oil-gas pipeline, a variety of solid surfaces coexist such as the pipe wall, asphaltene particles, wax crystal particles and sand particles entrained in the production fluids. These solid surfaces have different hydrophobicity and provided complex environment for the dynamic evolution of methane hydrate. There are increasing interest on the dependence of gas hydrate formation on the surface hydrophobicity, but contradictory results have been reported so far. For example, some studies showed that the hydrophobic surfaces were able to promote gas hydrate formation due to the tetrahedral ordering of water structure and the increased gas density at the solid-water interfaces (Li and Wang, 2015; Wang et al., 2015; Nguyen et al., 2017; Filarsky et al., 2019a). By contrast, the hydrophilic surfaces tend to inhibit hydrate formation due to the distorted water structure and the decreased gas density at the solid-water interface (Wang et al.,

2019). However, Filarsky et al. (2019b) demonstrated that a high-water-to-hydrate conversion was only obtained when slightly hydrophobic solids were present while both strongly hydrophilic or strongly hydrophobic solids inhibited methane hydrate formation. Moreover, Cox et al. (2018) indicated that methane hydrate information was insensitive to the presence of hydrophobic or hydrophilic solid surfaces. One of the possible reasons for the varied findings might be the different experimental conditions, such as the size of the solid particle and chemical groups of the surface coatings which also influence hydrate growth, used in different studies. The molecular mechanisms underlying the experimental observations is not thoroughly understood, which demands future works to elucidate the role of the intrinsic hydrophobicity of the solid surface on the growth and disassociation kinetics of methane hydrate.

Accordingly, the thermal stability of methane hydrates at various temperatures was investigated in the present study using MD simulation. Random solid surfaces with various roughness and hydrophobicity were constructed in order to gain insights into the effects of roughness and hydrophobicity on the methane hydrate dissociation kinetics, the gas bubble nucleation during hydrate dissociation and the free energy of hydrate adhesion to the rough solid surface.

2. Methodology

2.1 Molecular models

Force field: Molecular dynamics simulation is a method based on force field which contains mathematical functions predicting the structural, vibrational and thermo-

physical properties for substances in the model system (Wu and Coulon, 2016). In this study, the all-atom optimized potentials for liquid simulations (OPLS-AA) force field was used to describe the bonded (e.g., bond, angle and dihedral angle) and non-bonded (e.g., van der Waals and electrostatic interactions) parameters of all atoms (Kaminski et al., 2001). Water was described by the TIP4P model and methane was described by the united-atom model (Jorgensen et al., 1983).

Rough solid surface model: The Weierstrass-Mandelbrot (W-M) function which could be used to mimic the real rough surface topography was applied to construct the random surface with different roughness (Kulesza and Bramowicz, 2014):

$$z(x,y) = L\left(\frac{G}{L}\right)^{D-2}\left(\frac{ln\gamma}{M}\right)^{1/2}\sum_{m=1}^{M}\sum_{n=0}^{n_{max}}\gamma^{(D-3)n}\left\{\cos(\phi_{mn}) - \cos\left[\frac{2\pi\gamma^n(x^2+y^2)^{1/2}}{L}\cdot \cos\left(\tan^{-1}\left(\frac{y}{x}\right) - \frac{\pi m}{M}\right) + \phi_{mn}\right]\right\} \quad (1)$$

$$n_{max} = int\left[log_\gamma\left(\frac{L}{L_s}\right)\right] \quad (2)$$

where $z(x,y)$ is the height at the position of (x,y), L is the surface length, G is the altitude coefficient which is fixed at 2, D is the fractal dimensions, □□is the density of frequencies which is fixed at 1.5, γ^n represents the frequency of the n^{th} surface layer, M is the number of multiply ridge which is set at 10, L_s is the cut-off length which is fixed at 0.002, and ϕ_{mn} is a random phase array uniformly distributed in the interval of $[0, 2\pi]$. Random surfaces with two different morphology were evaluated by setting the parameters D as 2.75 and 2.77, respectively. The corresponding roughness (R) of these two types of surfaces were 0.36 nm and 0.48 nm, respectively.

Before building the molecular model for the rough surface, a body-centered cubic crystal (lattice constant: 2.86 Å) unit cell was used to generate a smooth solid surface

(6.897 nm × 5.160 nm × 1.003 nm). Based on the smooth surface, particle pillars were moved equidistantly with the z coordinate of the top particle equaled to the calculated result of the W-M function at the same (x, y) position. Subsequently, we adjusted the non-bonded solid-water interaction parameter (ε_{sw}) from 2.73 to 5.74 kJ mol^{-1} to modify the hydrophobicity of the solid surfaces. Basically, the maximum value of ε_{sw} of was set as 5.74 kJ mol^{-1} according to the hydrophilicity of iron (Morita et al., 2008). This value was then decreased to decrease the affinity of the solid surface to water, because the smaller value represents stronger hydrophobicity (Chowdhury et al., 2017). Overall twelve simulation scenarios with different solid surface roughness (R = 0, 0.36 and 0.48 nm) and surface hydrophobicity (ε_{sw}= 5.74, 4.73, 3.73, 2.73 kJ mol^{-1}) were designed to investigate the stability of hydrate cages.

Methane hydrate cluster model: Gas hydrate have many structure types and the three most common types exist in nature are sI, sII and SH hydrates (Sloan and Koh, 2007). Since the methane prefers to form sI hydrate, the geometry-optimized sI structure methane hydrate unit cell was obtained from Lenz and Ojamaë (2011) and used in this study. The unit cell was replicated along the x, y and z directions to form a 3 × 3 × 3 super cell to represent a cubic hydrate cluster according to Wu et al. (2019).

Model system: The initial model system was established by locating the methane hydrate cluster on the top of the rough solid surface (Fig. 1). In order to simulate an aqueous environment, the methane hydrate cluster was immersed in the liquid box containing methane (molecular number: 180) and water (molecular number: 4286 ~

178 4493). The corresponding methane concentration in the aqueous phase was about 0.04
179 mol mol^{-1}.

180 **2.2 Molecular dynamics simulation**

181 The initial model systems were energy minimized using the steepest descent algorithm,
182 which was equilibrated at NVT (constant number of atoms, volume and temperature)
183 and NPT (constant number of atom, pressure and temperature) ensemble, respectively,
184 in order to allow the system to reach the desired temperature (245, 250, 255 and 260K)
185 and pressure (500 bar). Subsequently, MD simulations were performed for 100
186 nanoseconds (ns) at NPT ensemble. The positions of the solid surface atoms were kept
187 restrained during the simulations. Leap-frog algorithm with a time-step of 1 fs was used
188 as the integrator to calculate the stochastic dynamics of molecules (Van Gunsteren and
189 Berendsen, 1988). The temperature and pressure were controlled by the V-rescale
190 thermostat and Berendsen barostat, respectively (Berendsen and Van Gunsteren, 1984;
191 Bussi et al., 2007). The cut-off of short-range interactions was set at 1.2 nm, whereas
192 the Particle Mesh Ewald (PME) algorithm was used to calculate the long-range
193 electrostatics interactions (Darden et al., 1993). Three-dimensional periodic boundary
194 condition (PBC) was applied throughout the simulations, which defined that when one
195 molecule diffused across the boundary of the simulation box it reappeared on the
196 opposite side (Sharma, 2019). By implementing PBC, the edge effects could be avoided
197 as each molecule always interacted with its neighbor molecules even though they were
198 close to the edge of the simulation box. All the simulations were performed using the
199 open source software Gromacs 5.0.5 (Van Der Spoel et al., 2005).

200 **2.3 Data analysis**

201 The face-saturated incomplete cage analysis method was used for data analysis (Guo et
202 al., 2011). The hydrate cages were classified as complete cage (CC) or incomplete cage
203 (IC) according to edge-saturated index (ζ_V) and face-saturated index (ζ_E):

204 $$\zeta_V \zeta_E = \frac{n_V^{E3+}}{n_V} \frac{n_E^{F2}}{n_E} \quad (3)$$

205 where n_V is the number of water molecules enclosing the void of water cages, n_V^{E3+}
206 is the number of cage waters shared with at least three cage edges, n_E is the number
207 of edges and n_E^{F2} is the number of edges shared with two cage faces. $\zeta_V \zeta_E = 1$
208 represents a complete cage with both edge-saturated and face-saturated. $\zeta_V \neq 1$ and
209 $\zeta_E = 1$ indicates a face-saturated incomplete cage (FSIC). The number of total cages
210 is the sum of the amount of CC and FSIC. The separating distance between the absorbed
211 methane and the adsorption site of a hydrate cage face is less than 3 Å, whereas the free
212 methane is more than 3 Å away of an adsorption site (Guo et al., 2011). The cage
213 structure was displayed using the algorithm provided by Jacobson et al. (2009). The
214 stability of methane hydrate above the solid surface with different hydrophobicity under
215 different temperatures was characterized by calculating the total number of hydrate
216 cage, the ratio of adsorbed methane and the free methane. The final values of these
217 parameters were determined by the average of the last 10 ns of the simulations.
218 The potential mean force (PMF) profiles of the adhesion of hydrate to solid surface
219 were obtained using the umbrella sampling method (Kästner, 2011). The oxygen atoms
220 of water and the methane molecules in the methane hydrate cage were position

restrained to avoid the collapse of the cage structure with a force constant of 1000. Around 50 windows for each system were selected for umbrella sampling. All the configurations were equilibrated under the NPT ensemble, after which MD production simulations were performed using the same settings. The PMF was calculated from unbiased probability distributions of the systems with the weighted histogram analysis method (Kumar et al., 1992).

3. Results and Discussion

3.1 Stability of hydrate cages on smooth surface with different hydrophilicity

The evolution of the number of methane hydrate cages above the smooth surface with varied hydrophobicity under different temperature is shown in Fig. 2. When the surface was highly hydrophilic (ε_{sw}: 5.74 kJ mol^{-1}), the number of methane hydrate cages almost doubled during the initial 40 ns and then kept stable with minor fluctuation under low temperature (245 K). The overall tendency was similar when the temperature increased to 255 K, but the hydrate growth rate became much slower. As shown in Fig. 2a, the number of methane hydrate cages only increased from 86 to 129 during the initial 40 ns which then slowly increased to 150 at the end of simulation at 255 K. The hindered growth rate at 255 K might be attributed to the thermal interference on the aggregation of cage-like water clusters or the ordered arrangement of gas molecules. The latter one might not be the predominant mechanism in context of the present study, which could be supported by the evolution of the number of the adsorbed methane throughout the simulation. According to the cage adsorption hypothesis, the strong

attractive interaction between dodecahedral water cages and methane molecules was the intrinsic driving force controlling methane hydrate formation (Guo et al., 2009). Our results demonstrated that the percentage of the methane adsorbed on the cage surface differed little when the temperature increased from 245 K to 255 K, suggesting that such temperature did not significantly influence the collective arrangement of methane molecules for hydrate formation (Fig. 3a). Accordingly, the observed slow rate of hydrate growth at 255 K was more likely attributed to the hindered adjustment of water molecules around the ordered arranged gas molecules according to the local structuring hypothesis (Radhakrishnan and Trout, 2002). The hydrate cluster became unstable once the temperature exceeded 255 K. As shown in Fig. 2a, the number of methane hydrate cages spontaneously decreased by 85% within 23 ns at 260 K, indicating the fast collapse of the hydrate structure and the break-up of cage linkages. The overall tendency of hydrate cage evolution was similar when ε_{sw} decreased from 5.74 to 4.73 and 3.73 kJ mol^{-1}, respectively. In these cases, the hydrate cages maintained stable below 255 K and started to disassociate at 260 K although the total number of hydrate cages varied with the hydrophobicity (Figs. 2b and 2c). When ε_{sw} was 4.73 kJ mol^{-1}, the final number of hydrate cages decreased by 23% when the temperature increased from 245 K to 255 K (Fig. 2b), but little difference was found in the ratio of the adsorbed methane at such temperature range (Fig. 3b). Similar tendency was observe when ε_{sw} decreased to 3.73 kJ mol^{-1}. As shown in Figs. 2c and 3c, the temperature rising from 245 K to 255 K resulted in 31% decrease in the total hydrate cages but did not change the fraction of the adsorbed methane. As aforementioned, this

finding demonstrated that a weak temperature driving force was unfavorable for the water molecules to adjust into cage-like water clusters, but allowed the adsorption of methane on the surfaces of hydrate cages. This could prolong the lifetime of hydrate cluster and allow the gradual formation of hydrate cages (Walsh et al., 2009). Under relatively higher temperature, the effect of surface hydrophobicity on the hydrate stability remained slight. The final number of hydrate cages at 255 K decreased by only 9% when ε_{sw} decreased from 5.74 to 3.73 kJ mol^{-1} (Figs. 2a and 2c). The surface hydrophobicity could potentially affect the rate of hydrate dissociation at 260 K but such change was non-monotonic. The hydrate cage dissociation time at 260 K was shortened from 20 to 13 ns when ε_{sw} decreased from 5.74 to 4.73 kJ mol^{-1} but rebounded to 20 ns when it further decreased to 3.73 kJ mol^{-1} (Figs. 2a, 2b and 2c).

The tendency of hydrate cage evolution changed significantly when ε_{sw} further decreased to 2.73 kJ mol^{-1}. As shown in Fig. 2d, the hydrate cluster was unable to remain stable even at 245 K. Although the number of hydrate cages doubled in the first 25 ns, it was followed by a continuously decrease until the end of simulation. The final number of hydrate cages was only 48% of that on the highly hydrophilic surface at 245 K (Figs. 2a and 2d). The destabilization effect became more obvious when the temperature exceeded 250 K. The hydrate cluster decomposed spontaneously and disappeared at 44 ns, 20 ns and 15 ns when the temperature increased to 250 K, 255 K and 260 K, respectively (Fig. 2d). Meanwhile, the ratio of the adsorbed methane declined fast even at very low temperature (Fig. 3d). For instance, the adsorbed methane almost disappeared within 40 ns at 250 K, indicating that all the methane escaped from

the hydrate surface. This might be attributed to the stronger interaction between the methane and the solid surface when the latter became highly hydrophobic, because Ma et al. (2020) demonstrated that a stronger guest-surface affinity would induce competitive adsorption for guest molecules between the surface and the hydrate which led to the decomposition of hydrate. Accordingly, it might be such competitive adsorption that decreased the ratio of methane adsorbed to hydrate cage faces and eventually destabilized the hydrate cluster on the hydrophobic surface.

3.2 Stability of hydrate cages on rough surface with different hydrophilicity

The final number of hydrate cages on hydrophilic (ε_{sw}: 5.74 kJ mol^{-1}) rough surface at low temperature differed slightly from that on smooth surface, but the hydrate growth rate significantly decreased with the surface roughness. For example, it took about 30 ns for the hydrate cluster to reach the size of 200 cages on a smooth surface at 245 K (Fig. 2a). However, it took 45 ns and 95 ns to achieve the same size on a surface of 0.36 nm and 0.48 nm roughness, respectively (Fig. 2e and 2i). Nevertheless, the number of the adsorbed methane did not reduce with the increase of surface roughness at 245 K (Fig. 4a). Moreover, the methane hydrate cages became much less stable on rough surface than on smooth surface when the temperature exceeded 245 K. For instance, the number of methane hydrate cages decreased by 10% and 22%, respectively, when the roughness of the solid surface increased from 0 to 0.36 nm and 0.48 nm at 255 K (ε_{sw}: 5.74 kJ mol^{-1}). When the temperature further increased to 260 K, the lifetime of methane hydrate cluster reduced from 23 ns to 15 ns by replacing the smooth surface with rough surfaces (Figs. 2a, 2e and 2i).

On the rough solid surface with weaker hydrophilicity (ε_{sw}: 3.73 ~ 4.73 kJ mol^{-1}), the hydrate was much less stable than on the smooth surface. For instance, the hydrate remained stable on the smooth surface when the temperature increased up to 255 K (Figs. 2b and 2c), but 60% of the hydrate cages broke up at 255 K when the roughness increased to 0.36 nm (Fig. 2f). The lower hydrophilicity, the faster the hydrate disassociated. The lifetime of the hydrate cluster at 255 K was shortened from 80 ns (Fig. 2f) to 25 ns (Fig. 2g) when ε_{sw} decreased from 4.73 to 3.73 kJ mol^{-1}.

However, the hydrate stability differed little during the increase of the roughness if the surface became hydrophobic (ε_{sw}: 2.73 kJ mol^{-1}). It could be evidenced by the overall evolution of the total number of hydrate cages, which demonstrated that the hydrate cages almost broke up in all these case at 250 K (Figs. 2d, 2h and 2l).

3.3 Gas bubble nucleation during hydrate cage decomposition on rough surface

Selected snapshots of gas bubble nucleation after the decomposition of methane hydrate cages on the solid surface with different hydrophobicity and roughness are provided (Fig. 6). When a smooth surface with relatively high hydrophilicity (ε_{sw}: 5.74 kJ mol^{-1}) was present, a distinct methane bubble nucleus was observed in the water above the surface at about 24 ns (Fig. 6a). The bubble's size increased by gathering the free methane molecules dispersed in the water and maintained a spherical shape at the end of simulation (Figs. 6c). The gas bubble did not contact with the solid surface throughout the simulation since there was always a water film between the bubble and solid surface. The thickness of the water film decreased with time and kept stable at about ~ 0.7 nm at the end of simulation (Fig. 6c). The overall evolution of methane

bubble was similar when the surface roughness increased to 0.36 nm (Figs. 6d-6f) and 0.48 nm (Figs. 6g-6i), respectively, if ε_{sw} was fixed at 5.74 kJ mol^{-1}. In these cases, the methane bubble started to nucleate in the water phase and then grew and swam in the water. Although the methane bubble was very close to the solid surface with high roughness at the end of simulation, it remained spherical in shape with a diameter of ~ 3.0 nm without adsorption on the rough surface (Figs. 6g-6i). The aforementioned water layer still existed below the lowest edge of the bubble (Fig. 6i).

The nucleation site of the gas bubble varied with the surface roughness when the surface hydrophilicity decreased (ε_{sw}= 3.73 ~ 4.73 kJ mol^{-1}). For instance, the gas bubble also started to nucleate in the water when the roughness was no more than 0.36 nm (data not shown). However, it preferred to nucleate on the solid surface when the surface was highly rough (R: 0.48 nm), which adsorbed and grew on the convex area of the solid surface without moving into the groove or suspended in the water phase (Figs. 6j-6O). The water near the solid surface was expelled by the gas bubble, therefore, the aforementioned water film below the gas bubble was not observed throughout the hydrate disassociation (Figs. 6j'-6l').

When ε_{sw} was further decreased to 2.73 kJ mol^{-1}, the surface became strongly hydrophobic and inhibited the formation of methane bubble on both the smooth and rough surfaces. To shed further insights into this finding, the gas aggregation process was characterized by the profile of the methane density along the distance from the solid surface at different time during hydrate dissociation (Fig. 7d). The methane molecules were mainly located at 2.3 to 4.8 nm from the solid surface before the hydrate

started to dissociate, which represented the methane trapped in the hydrate cages. Only free and scattered methane molecules existed near the surface as the density of the methane located at about 1.2 nm from the solid surface was less than 80 kg m^{-3} (Fig. 7d). However, the density of methane near the surface steeply increased to 252 kg m^{-3} after the hydrate disassociated for 10 ns and finally rose to 400 kg m^{-3} at the end of simulation (100 ns). The methane density was almost zero in the bulk water region at the end of hydrate dissociation (Fig. 7d). This process of density change clearly demonstrated the fast adsorption of the released methane to the solid surface after hydrate dissociation. The methane molecules flatly laid on the solid surface instead of forming gas bubble (Fig. 7a). The tendency of density evolution was similar when the surface roughness increased to 0.36 nm and 0.48 nm (Figs. 7e and7f), respectively, where the methane was spread and deposited in the groove area of the rough surface without forming gas bubble (Figs. 7b and 7c). This phenomenon might be attributed to the strong hydrophobic attractions between methane and the solid surface. This was consistent with Nguyen et al. (2020) which indicated that the dissolved gas molecules would populate at the interface between water and hydrophobic solid surface.

3.4 Free energy of hydrate cage adhesion onto rough surface

Rough surface was much more energetically favorable for the hydrate cage adsorption compared with the smooth surface when the surface was hydrophilic (Fig. 8). The PMF slightly increased as the distance between the hydrate cage and the smooth surface (ε_{sw}: 5.74 kJ mol^{-1}) decreased from 1.3 nm to 0.7 nm, which was followed by the appearance of two peaks at 0.5 nm and 0.2 nm, respectively, during the approaching process (Fig.

375 8a). This suggested the existence of energy barriers (~ 0.8 kJ mol^{-1}) that the hydrate
376 cage needed to overcome before it could successfully reach the smooth solid surface.
377 By contrast, the hydrate cage could spontaneously deposit onto the groove of the rough
378 surface, which was evidenced by the obvious energy drop (~ 3.3 kJ mol^{-1}) when the
379 distance between the hydrate cage and the rough surface decreased from 0.5 to 0.3 nm
380 (Fig. 8b).
381 Another clear finding from the PMF results was that the energy barrier for the
382 adsorption of hydrate cage onto the smooth surface became less or even disappeared
383 when the surface became hydrophobic. For example, only one small peak was found in
384 the PMF curve when the hydrate cage moved from 1.3 to 0.65 nm from the smooth
385 surface when ε_{sw} equaled 4.73 kJ mol^{-1}. Subsequently, a continuous drop (~ 2.6 kJ
386 mol^{-1}) appeared in the PMF curve, indicating a spontaneous hydrate cage deposition
387 (Fig. 8a). Such peak disappeared when ε_{sw} further decreased to 3.73 kJ mol^{-1}. Instead,
388 the PMF kept decreasing when the hydrate cage moved toward the smooth surface until
389 reaching the minimum value when their distance was about 0.2 nm. It suggested that
390 the hydrate cage adsorption in this case could spontaneously occur while the overall
391 free energy for the adsorption process was about 1.8 kJ mol^{-1}.
392 However, the tendency for the adsorption of hydrate cage on rough surface was
393 opposite when the surface changed from hydrophilic to hydrophobic. From the energy
394 point of view, the higher hydrophobicity, the more difficult for the hydrate cage to
395 approach the rough surface. As shown in Fig. 8b, the overall free energy for hydrate
396 cage adsorption decreased by ~70% when ε_{sw} decreased from 5.74 to 4.73 kJ mol^{-1}.

It even became energy unfavorable for the hydrate cage to deposit onto the rough surface when ε_{sw} decreased to 3.73 kJ mol^{-1}. Particularly, three peaks were observed at about 0.9 nm, 0.6 nm, and 0.3 nm, respectively, in the PMF curve during the approaching of hydrate cage to the rough surface when ε_{sw} was 3.73 kJ mol^{-1}. The largest energy barrier that the hydrate cage needed to overcome was up to 2 kJ mol^{-1} when it moved from 0.5 to 0.3 nm from the rough surface before it could successfully deposit onto the groove of the rough steel surface (Fig. 8b).

4. Conclusions

This study demonstrated that the thermal stability of methane hydrate was highly dependent on the roughness and intrinsic hydrophobicity of the solid steel surface. The gas transportation would become safer if the hydrophobicity of the pipeline wall surface increased, because the methane hydrate could remain stable at 255 K on a hydrophilic surface (ε_{sw}: 5.74 kJ mol^{-1}) but completely dissociate at 250 K on a hydrophobic surface (ε_{sw}: 2.73 kJ mol^{-1}). The less hydrate stability on hydrophobic surface might be attributed to the competitive adsorption of methane molecules which drove the escape of methane from the hydrate surface to the hydrophobic surface and eventually facilitated the hydrate decomposition. The hydrates also became less stable on rough surface than on smooth surface, which was evidenced by the faster broke up of hydrate cages and the shortened lifetime of hydrate cages. Under the stable conditions, the free energy for the adhesion of hydrates to the solid surface also varied with the roughness and hydrophobicity. On the hydrophilic surface, the hydrate could spontaneously deposit onto the rough solid surface, but it needed to overcome about 0.8 kJ mol^{-1}

energy barrier before adhered to the smooth surface. Such tendency was opposite on the hydrophobic surface. The smooth surface was more energetically favorable for the hydrate adsorption while the largest energy barrier for approaching the rough surface was 2 kJ mol^{-1}. Overall findings suggested that it was possible to decrease the hydrate stability and increase the resistance for hydrate adhesion by increasing the roughness and hydrophobicity of the pipe wall to mitigate flow assurance issues. Future works are required to test the adhesion strength between gas hydrate and pipeline steel with different surface properties using high-pressure micromechanical force apparatus and validate the model in the multi-phase flow pipeline.

Acknowledgement

This study was financially supported by Shenzhen Science and Technology Program (No. GJHZ20200731095600002, No. JCYJ20210324140810027), Guangdong Basic and Applied Basic Research Foundation (No. 2022A1515011834), National Key Research and Development Program of China for Young Scientist (No. 2021YFF0502300), Key Special Project for Introduced Talents Team of Southern Marine Science and Engineering Guangdong Laboratory (Guangzhou) (No. GML2019ZD0403 and No. GML2019ZD0401), and Stable Support Funding from the Science, Technology and Innovation Commission of Shenzhen Municipality (No. WDZC20200818183253001).

References

Berendsen, H., Van Gunsteren, W., 1984. Molecular dynamics simulations: Techniques and approaches. Molecular Liquids. Springer, pp. 475-500.

Bussi, G., Donadio, D., Parrinello, M., 2007. Canonical sampling through velocity rescaling. J Chem Phys 126, 014101.

Chen, C., Hu, W., Yang, L., Zhao, J., Song, Y., 2021. Gas supersaturation and diffusion joint controlled CH_4 nanobubble evolution during hydrate dissociation. J Mol Liq 323, 114614.

Chowdhury, S.S., Pandey, P.R., Kumar, R., Roy, S., 2017. Effect of shape of protrusions and roughness on the hydrophilicity of a surface. Chem Phys Lett 685, 34-39.

Cox, S.J., Taylor, D.J.F., Youngs, T.G.A., Soper, A.K., Totton, T.S., Chapman, R.G., Arjmandi, M., Hodges, M.G., Skipper, N.T., Michaelides, A., 2018. Formation of methane hydrate in the presence of natural and synthetic nanoparticles. J Am Chem Soc 140, 3277-3284.

Darden, T., York, D., Pedersen, L., 1993. Particle mesh Ewald: An N·log (N) method for Ewald sums in large systems. J Chem Phys 98, 10089-10092.

Das, S., Tadepalli, K.M., Roy, S., Kumar, R., 2022. A review of clathrate hydrate nucleation, growth and decomposition studied using molecular dynamics simulation. J Mol Liq 348, 118025.

Filarsky, F., Schmuck, C., Schultz, H.J., 2019a. Development of a surface-active coating for promoted gas hydrate formation. Chem Ing Tech 91, 85-91.

461 Filarsky, F., Schmuck, C., Schultz, H.J., 2019b. Impact of modified silica beads on
462 methane hydrate formation in a fixed-bed reactor. Ind Eng Chem Res 58, 16687-
463 16695.
464 Guo, G.-J., Li, M., Zhang, Y.-G., Wu, C.-H., 2009. Why can water cages adsorb
465 aqueous methane? A potential of mean force calculation on hydrate nucleation
466 mechanisms. Phys Chem Chem Phys 11, 10427-10437.
467 Guo, G.J., Zhang, Y.G., Liu, C.J., Li, K.H., 2011. Using the face-saturated incomplete
468 cage analysis to quantify the cage compositions and cage linking structures of
469 amorphous phase hydrates. Phys Chem Chem Phys 13, 12048-12057.
470 Hu, P., Chen, D., Zi, M., **Wu, G.**, 2018. Effects of carbon steel corrosion on the
471 methane hydrate formation and dissociation. Fuel 230, 126-133.
472 Jacobson, L.C., Hujo, W., Molinero, V., 2009. Thermodynamic stability and growth of
473 guest-free clathrate hydrates: A low-density crystal phase of water. J Phys Chem
474 B 113, 10298-10307.
475 Ji, H., Chen, D., Zhao, C., **Wu, G.**, 2018. Molecular dynamics simulation of methane
476 hydrate formation and dissociation in the clay pores with fatty acids. J Phys
477 Chem C 122, 1318-1325.
478 Ji, H., **Wu, G.**, Zi, M., Chen, D., 2016. Microsecond molecular dynamics simulation
479 of methane hydrate formation in humic-acid-amended sodium montmorillonite.
480 Energ Fuel 30, 7206-7213.
481 Jorgensen, W.L., Chandrasekhar, J., Madura, J.D., Impey, R.W., Klein, M.L., 1983.
482 Comparison of simple potential functions for simulating liquid water. J Chem

Phys 79, 926-935.

Kaminski, G.A., Friesner, R.A., Tirado-Rives, J., Jorgensen, W.L., 2001. Evaluation and reparametrization of the OPLS-AA force field for proteins via comparison with accurate quantum chemical calculations on peptides. J Phys Chem B 105, 6474-6487.

Kästner, J., 2011. Umbrella sampling. Computational Molecular Science 1, 932-942.

Kuang, Y., Feng, Y., Yang, L., Song, Y., Zhao, J., 2019. Effects of micro-bubbles on the nucleation and morphology of gas hydrate crystals. Phys Chem Chem Phys 21, 23401-23407.

Kulesza, S., Bramowicz, M., 2014. A comparative study of correlation methods for determination of fractal parameters in surface characterization. Appl Surf Sci 293, 196-201.

Kumar, S., Rosenberg, J.M., Bouzida, D., Swendsen, R.H., Kollman, P.A., 1992. The weighted histogram analysis method for free-energy calculations on biomolecules. I. The method. J Comput Chem 13, 1011-1021.

Lenz, A., Ojamäe, L., 2011. Structures of the I-, II-and H-methane clathrates and the ice- methane clathrate phase transition from quantum-chemical modeling with force-field thermal corrections. J Phys Chem A 115, 6169-6176.

Li, H., Wang, L., 2015. Hydrophobized particles can accelerate nucleation of clathrate hydrates. Fuel 140, 440-445.

Ma, R., Zhong, H., Li, L., Zhong, J., Yan, Y., Zhang, J., Liu, J., 2020. Molecular insights into the effect of a solid surface on the stability of a hydrate nucleus. J

505 Phys Chem C 124, 2664-2671.
506 Morita, Y., Onodera, T., Suzuki, A., Sahnoun, R., Koyama, M., Tsuboi, H.,
507 Hatakeyama, N., Endou, A., Takaba, H., Kubo, M., 2008. Development of a new
508 molecular dynamics method for tribochemical reaction and its application to
509 formation dynamics of MoS_2 tribofilm. Appl Surf Sci 254, 7618-7621.
510 Nguyen, N.N., Galib, M., Nguyen, A.V., 2020. Critical review on gas hydrate
511 formation at solid surfaces and in confined spaces-why and how does interfacial
512 regime matter? Energ Fuel 34, 6751-6760.
513 Nguyen, N.N., Nguyen, A.V., Steel, K.M., Dang, L.X., Galib, M., 2017. Interfacial
514 Gas Enrichment at Hydrophobic Surfaces and the Origin of Promotion of Gas
515 Hydrate Formation by Hydrophobic Solid Particles. J Phys Chem C 121, 3830-
516 3840.
517 Radhakrishnan, R., Trout, B.L., 2002. A new approach for studying nucleation
518 phenomena using molecular simulations: Application to CO_2 hydrate clathrates. J
519 Chem Phys 117, 1786-1796.
520 Sharma, S., 2019. Molecular Dynamics Simulation of Nanocomposites Using
521 BIOVIA Materials Studio, Lammps and Gromacs. Elsevier.
522 Shi, B., Song, S., Chen, Y., Duan, X., Liao, Q., Fu, S., Liu, L., Sui, J., Jia, J., Liu, H.,
523 Zhu, Y., Song, C., Lin, D., Wang, T., Wang, J., Yao, H., Gong, J., 2021. Status of
524 natural gas hydrate flow assurance research in China: A Review. Energ Fuel 35,
525 3611-3658.
526 Sloan, E.D., Koh, C.A., 2007. Clathrate hydrates of natural gases. CRC press.

Uddin, M., Coombe, D., 2014. Kinetics of CH4 and CO2 Hydrate Dissociation and Gas Bubble Evolution via MD Simulation. J Phys Chem A 118, 1971-1988.

Van Der Spoel, D., Lindahl, E., Hess, B., Groenhof, G., Mark, A.E., Berendsen, H.J., 2005. GROMACS: fast, flexible, and free. J Comput Chem 26, 1701-1718.

Van Gunsteren, W., Berendsen, H., 1988. A leap-frog algorithm for stochastic dynamics. Mol Simulat 1, 173-185.

Walsh, M.R., Koh, C.A., Sloan, E.D., Sum, A.K., Wu, D.T., 2009. Microsecond simulations of spontaneous methane hydrate nucleation and growth. Science 326, 1095-1098.

Wang, J., Wang, R., Yoon, R.-H., Seol, Y., 2015. Use of hydrophobic particles as kinetic promoters for gas hydrate formation. J Chem Eng Data 60, 383-388.

Wang, R., Liu, T., Ning, F., Ou, W., Zhang, L., Wang, Z., Peng, L., Sun, J., Liu, Z., Li, T., Sun, H., Jiang, G., 2019. Effect of hydrophilic silica nanoparticles on hydrate formation: Insight from the experimental study. J Energ Chem 30, 90-100.

Wei, N., Pei, J., Li, H., Sun, W., Xue, J., 2022. Application of in-situ heat generation plugging removal agents in removing gas hydrate: A numerical study. Fuel 323, 124397.

Wu, G., Coulon, F., 2016. Modelling the environmental fate of petroleumhydrocarbons during bioremediation. in: McGenity, T.J. (Ed.). Hydrocarbon and Lipid Microbiology Protocols, Springer Protocols Handbooks. Springer, pp. 165-180.

Wu, G., Tian, L., Chen, D., Niu, M., Ji, H., 2019. CO_2 and CH_4 Hydrates:

549 replacement or cogrowth? J Phys Chem C 123, 13401-13409.
550 Yagasaki, T., Matsumoto, M., Andoh, Y., Okazaki, S., Tanaka, H., 2014. Effect of
551 bubble formation on the dissociation of methane hydrate in water: A molecular
552 dynamics study. J Phys Chem B, 1900-1906.
553 Zhang, W., Fan, S., Wang, Y., Lang, X., Li, G., 2021. Preparation and performance of
554 biomimetic superhydrophobic coating on X80 pipeline steel for inhibition of
555 hydrate adhesion. Chem Eng J 419, 129651.
556 Zhang, W., Fan, S., Wang, Y., Lang, X., Li, G., 2022. Development of a composite
557 structured surface for durable anti-hydrate and enhancing thermal conductivity.
558 Int J Heat Mass Tran 192, 122909.
559 Zi, M., Chen, D., **Wu, G.**, 2018. Molecular dynamics simulation of methane hydrate
560 formation on metal surface with oil. Chem Eng Sci 191, 253-261.
561

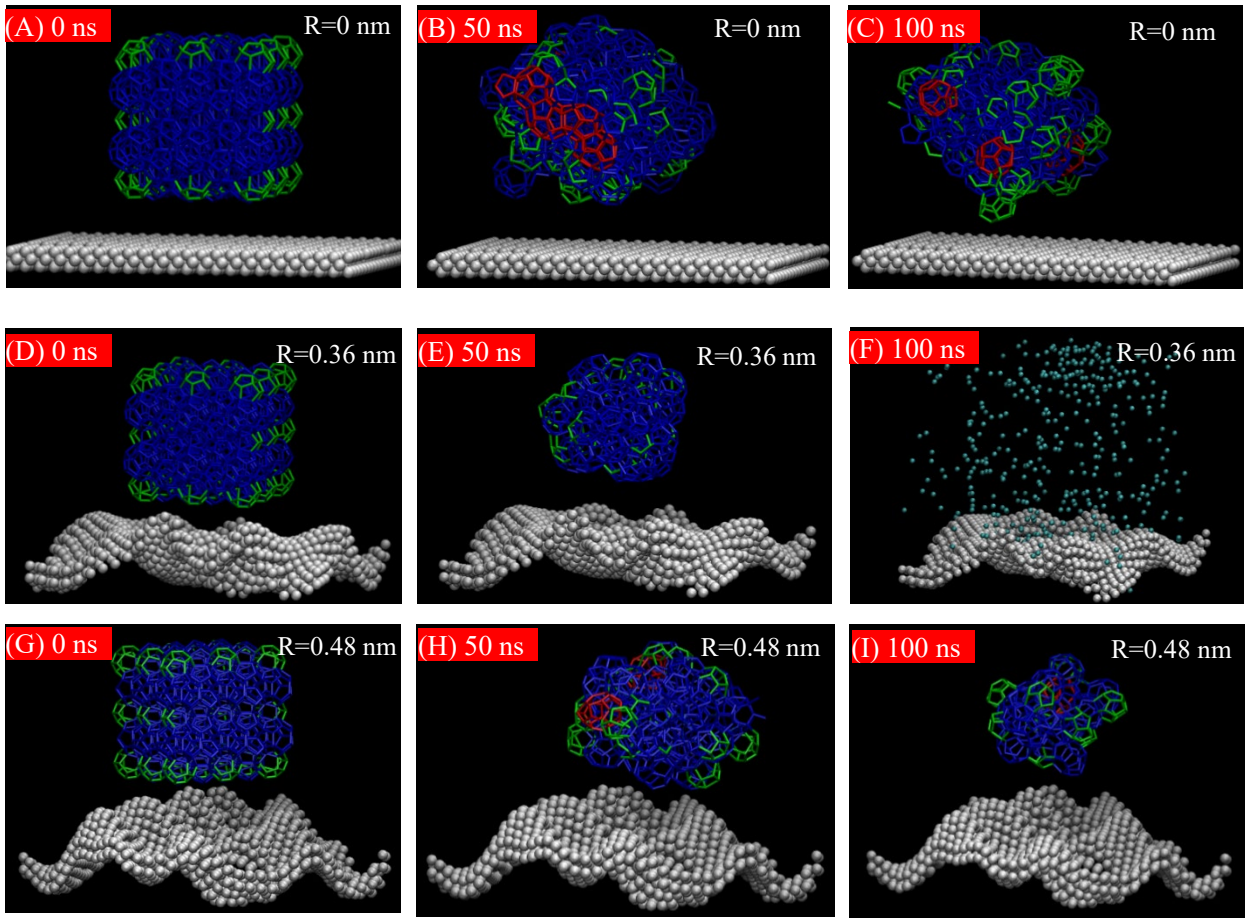

Fig. 1 Snapshots showing the evolution of methane hydrate clusters on solid surface with different roughness (T=255 K, ε_{sw}=4.73 kJ mol^{-1}). Solid surface: gray, 5^{12} cage: green, $5^{12}6^2$ cage: blue, $5^{12}6^3$ cage: red. Dispersed methane molecules (cyan balls) are only shown in panel F. The free water molecules are hidden in order to show the configurations of water cages more clearly.

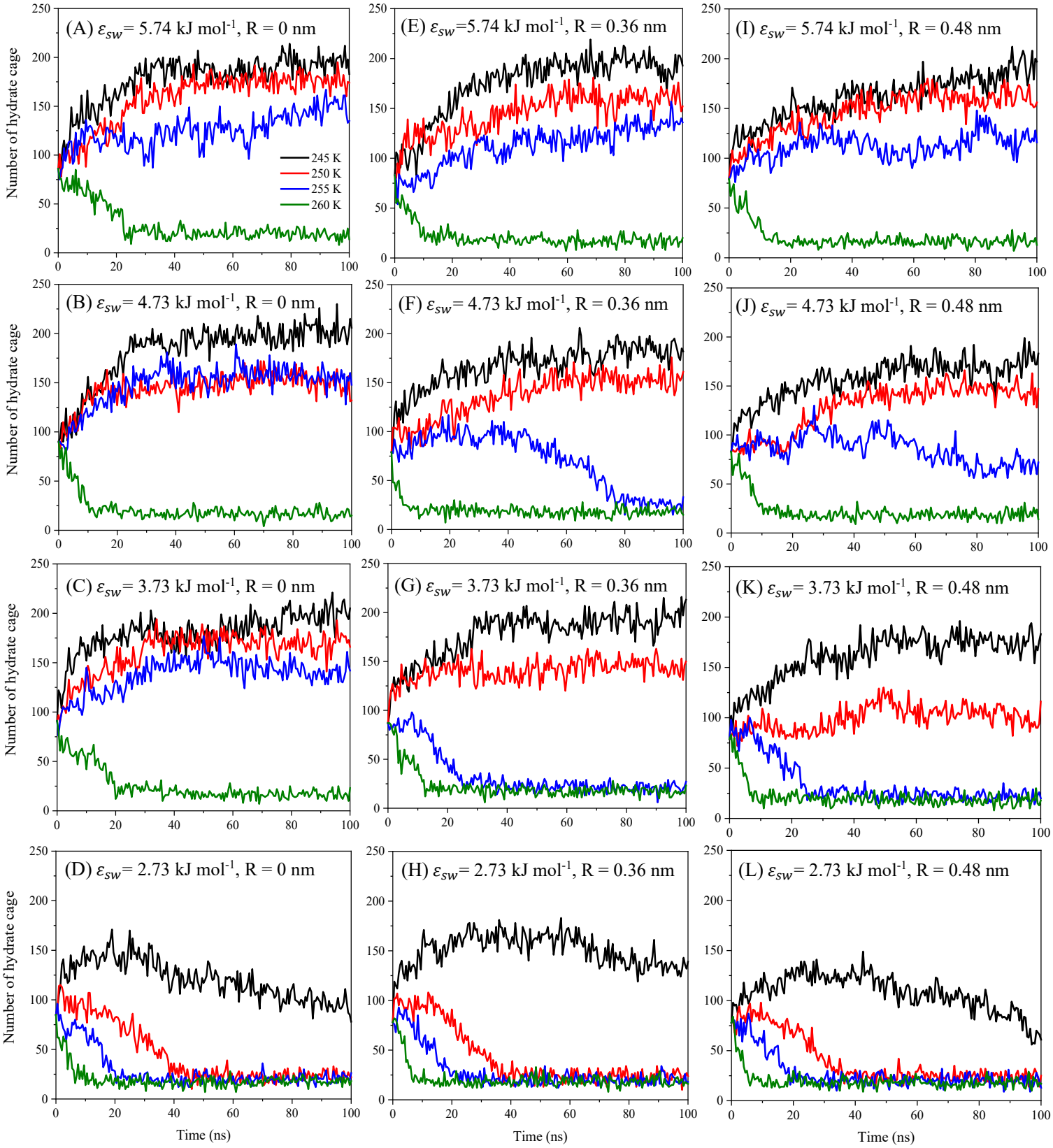

Fig. 2 Evolution of the number of methane hydrate cages on surfaces with different roughness and hydrophobicity

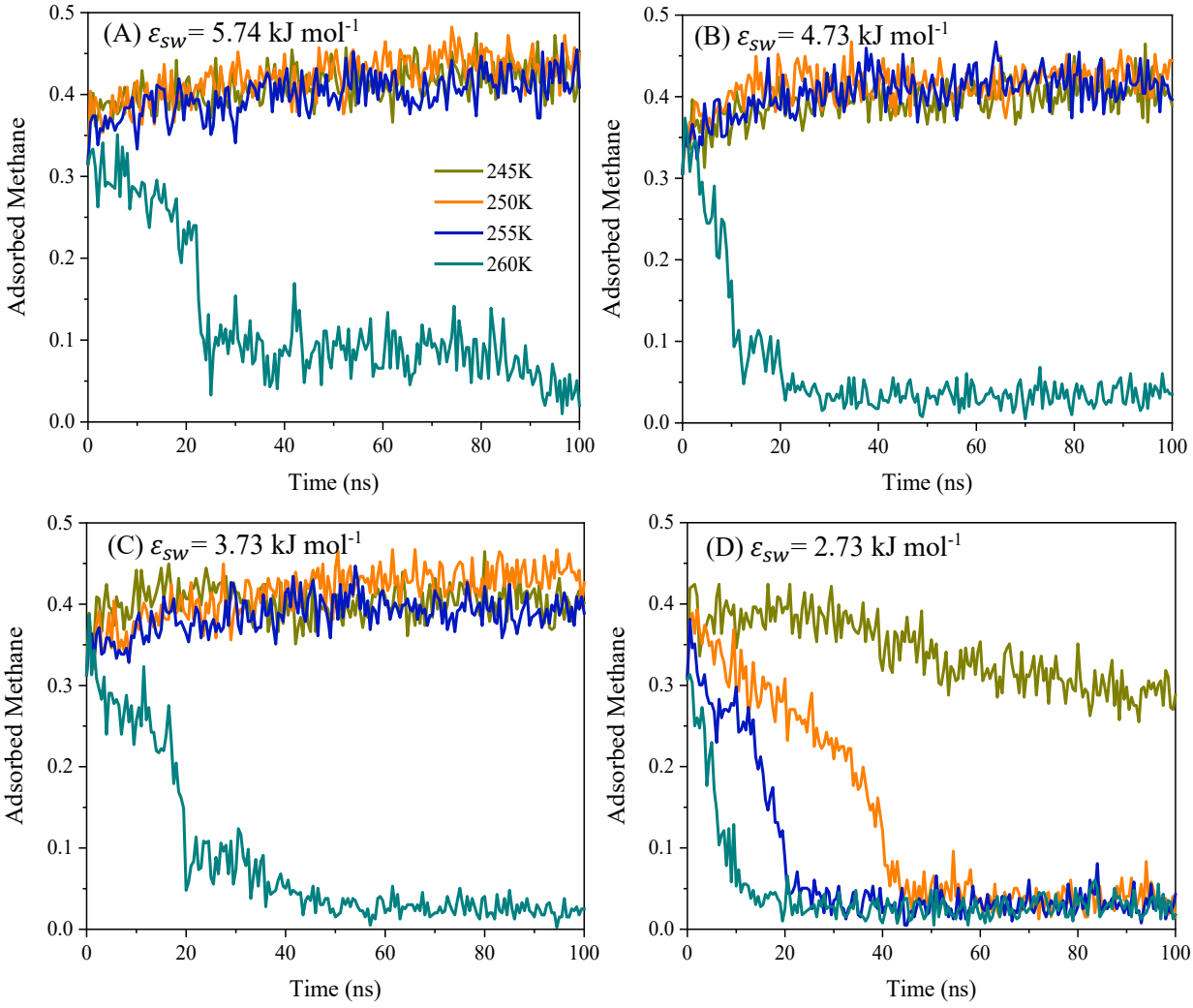

Fig. 3 Evolution of the ratio of adsorbed methane in the simulation systems containing smooth surface with different hydrophobicity

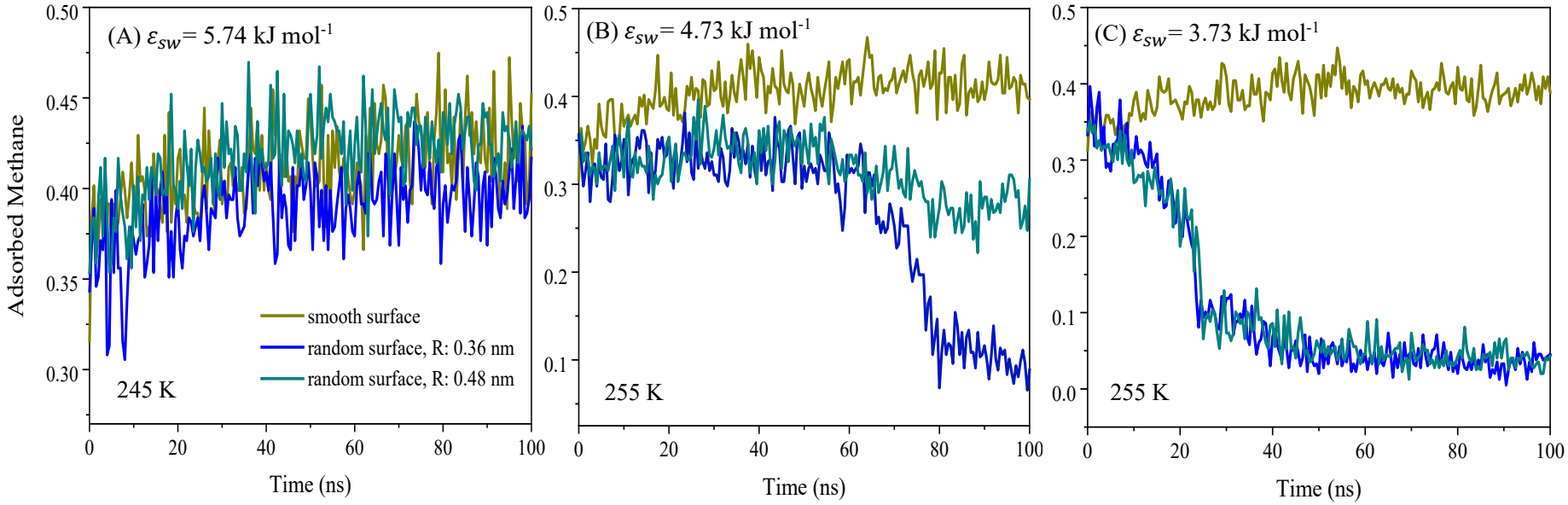

Fig. 4 Evolution of the ratio of adsorbed methane in the simulation systems containing rough surface with different hydrophobicity

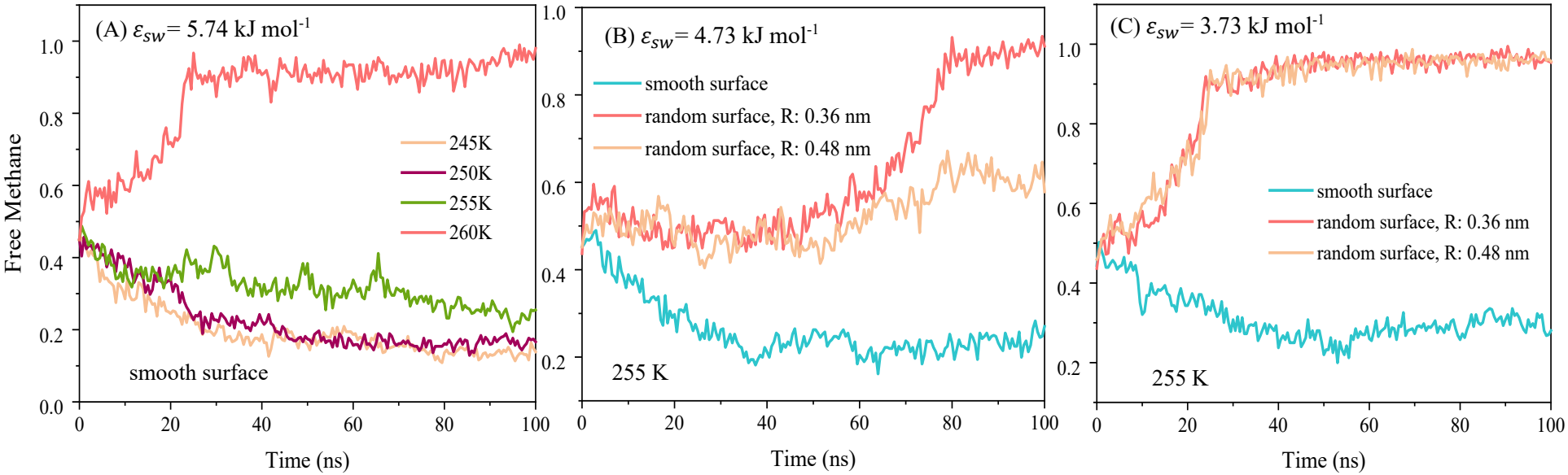

Fig. 5 Evolution of the ratio of free methane in different simulation systems

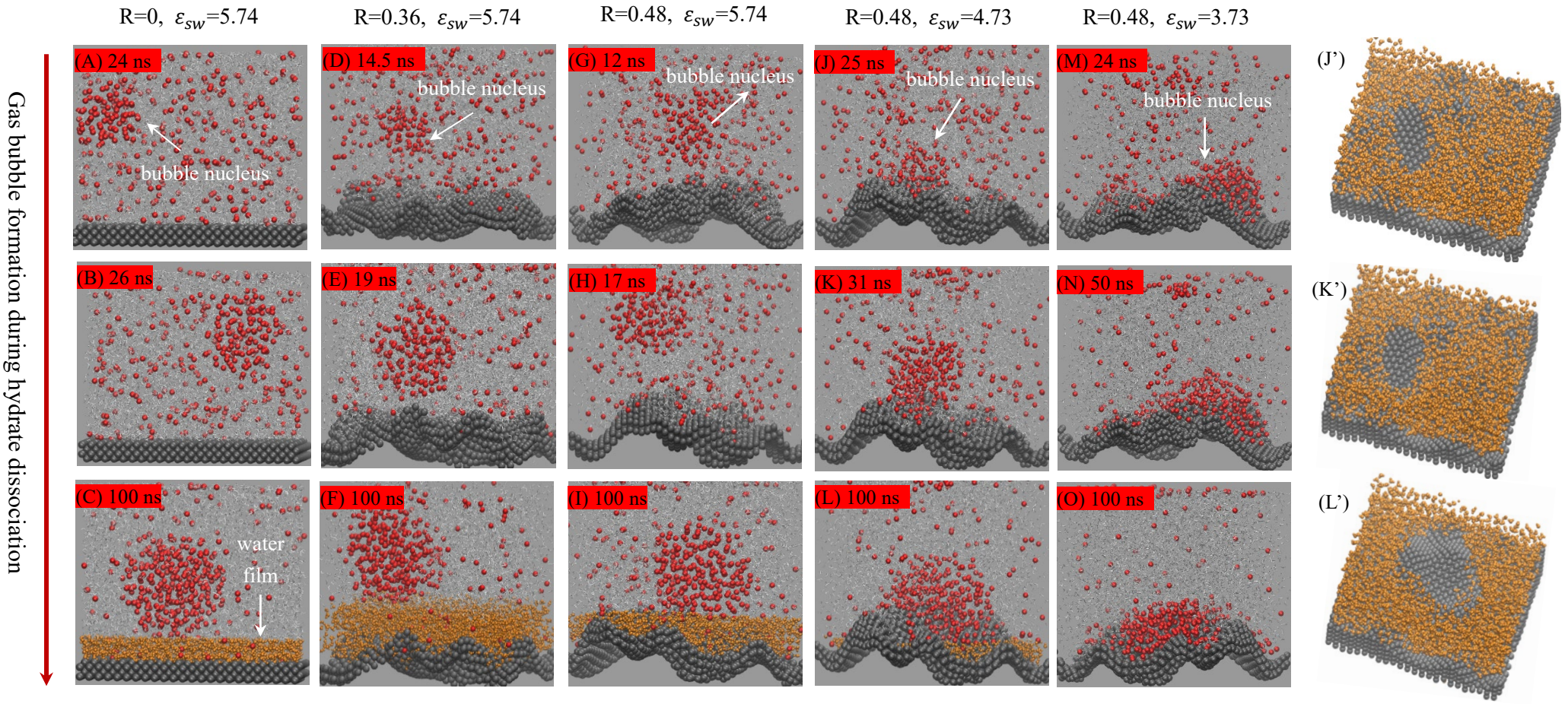

Fig. 6 Gas bubble evolution during hydrate dissociation on solid surfaces with various roughness (R: nm) and hydrophobicity (ε_{sw}: kJ mol^{-1}) at 260 K. Panel J'-L' is the vertical view of the water molecules below the gas bubble corresponding to J-L, respectively. Water film close to the substrate are highlighted in orange.

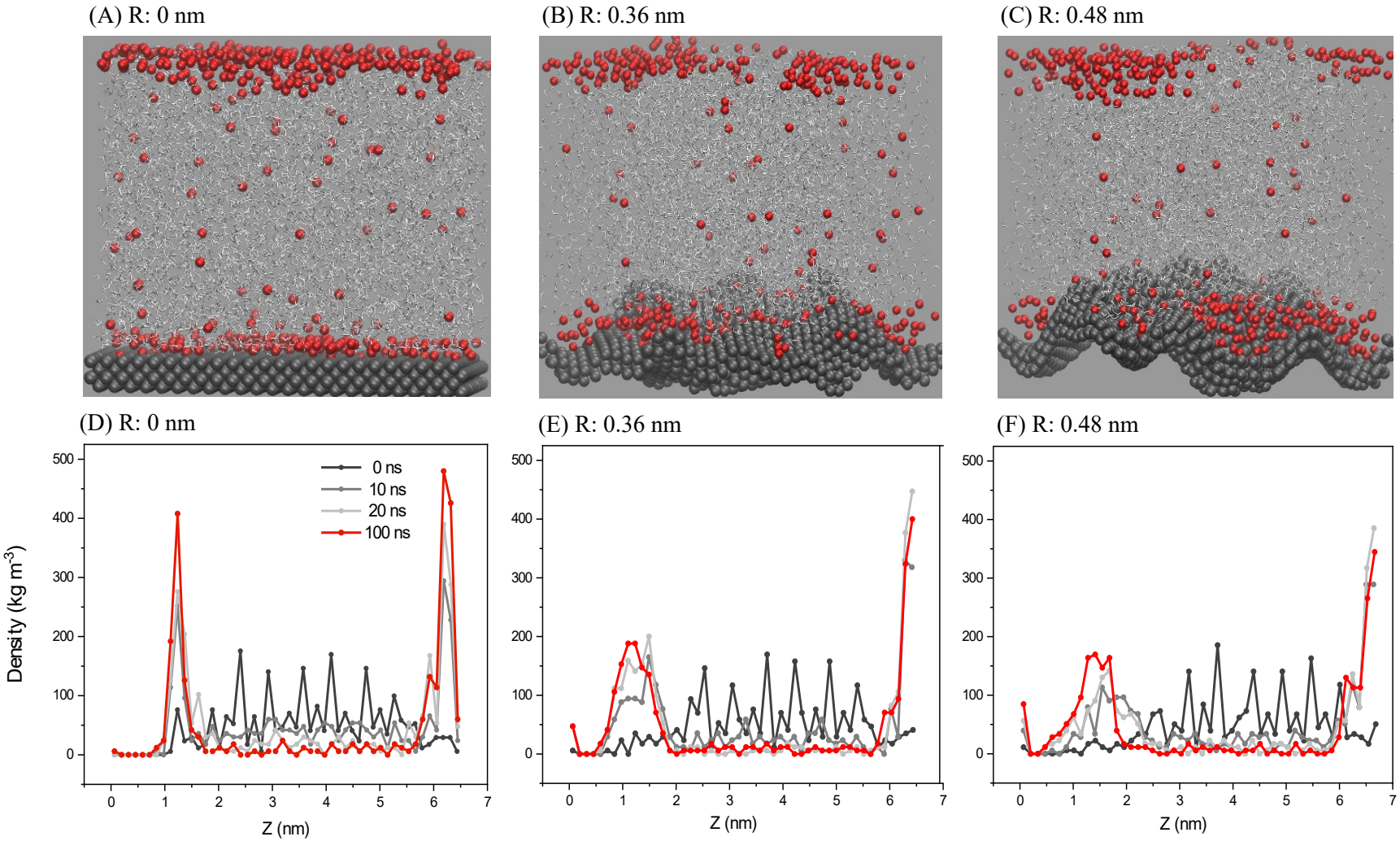

Fig. 7 Configuration of methane molecules on the solid surface with different roughness at the end of hydrate disassociation at 260 K. The temporal changes in the methane density are shown in Panels D-F where z represents the distance from the solid surface (ε_{sw}: 2.73 kJ mol^{-1}).

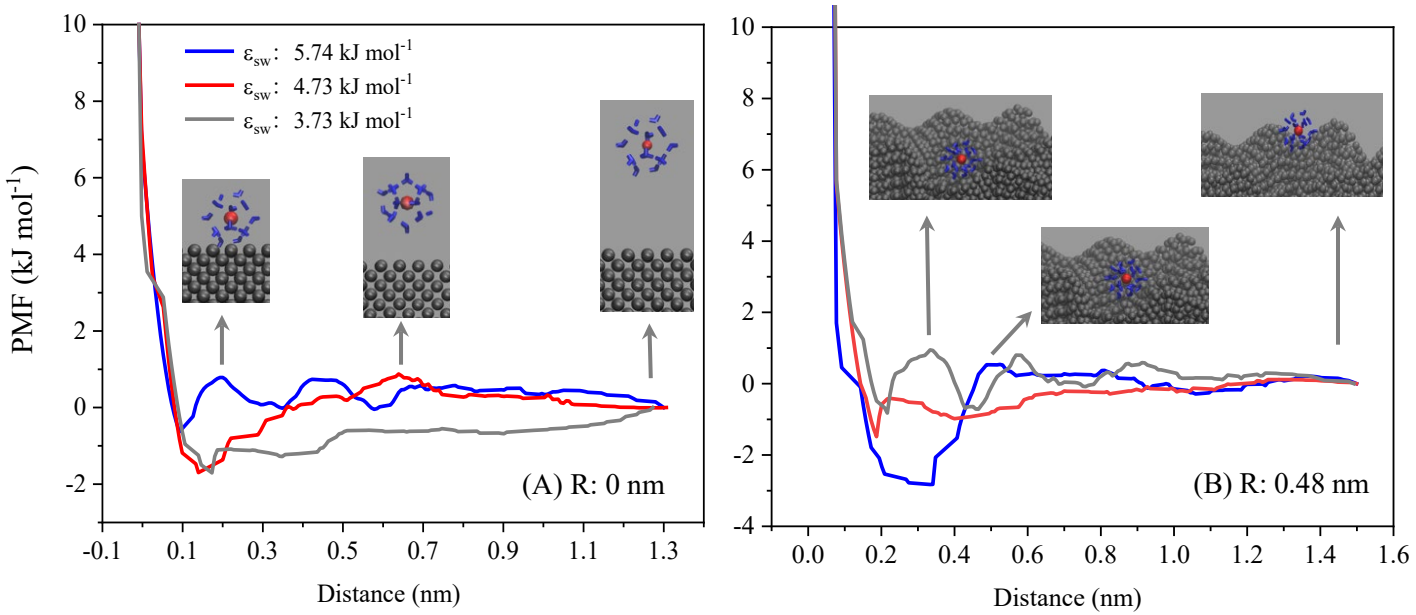

Fig. 8 Potential mean force during the adsorption of a methane hydrate cage onto the smooth and rough surface (250 K, 500 bar). The curves were smoothed using 30-points Savitzky-Colay method.